Advanced Composites and Hybrid Materials (2025) 8:303
https://doi.org/10.1007/s42114-025-01383-1

RESEARCH

Sustained virucidal functionality in practical-scale polymer matrices enabled by visible light-responsive Cu_xO–TiO_2 photocatalyst

Yujin Lee[1] · Kanghyun Lee[1] · Junhyeop Shin[2,3,4] · Seyoung Choi[2,3,4] · Seyeon Kim[1] · Geon Woo Kim[1] · Abraham Seo[1] · Jeong Woo Han[5] · Tae Yong Kim[1] · Inho Nam[2,3,4] · Soomin Park[1]

Received: 17 March 2025 / Revised: 17 June 2025 / Accepted: 24 June 2025

Abstract

The COVID-19 pandemic has highlighted the urgent need for durable and highly effective virucidal materials. This study presents a breakthrough by integrating Cu_xO–TiO_2 photocatalysts into widely used polymer matrices, such as silicone, polypropylene, and air filters, to achieve sustained antiviral functionality with practical applicability. Unlike previous studies that primarily focused on the antiviral efficacy of Cu-based photocatalysts, our study provides atomic-level insights into the regeneration of virucidal Cu_xO ($x > 1$) on TiO_2, strongly influenced by the local atomic structures of Cu_xO, particularly when Cu exhibits a low Cu–O coordination number (~3), as confirmed by X-ray absorption spectroscopy. This regeneration process is essential for high virucidal performance via interfacial charge transfer (IFCT) mechanisms. Our results show that Cu_xO–TiO_2 photocatalysts achieve an 8.67-ln reduction in viral activity within just 3 min of visible light exposure ($\lambda > 400$ nm). Furthermore, by optimizing the incorporation of Cu_xO–TiO_2 materials, we demonstrate that antiviral functionality is maintained in polymer matrices through strategic positioning of the photocatalysts near the surface. This ensures Cu_xO–TiO_2 remains accessible to light and reactants while maintaining strong polymer adhesion, which is critical for mechanical stability and durability. Not only does this polymer composite exhibit effective virucidal performance (4.28-ln reduction within 30 min), but it also ensures sustained performance (99.1% of its initial performance after 3 weeks under ambient conditions). These findings highlight the scalability and practical potential of these materials for consumer applications, significantly contributing to public health by reducing virus transmission.

Keywords Photocatalysis · Virucidal · Polymer matrices · Visible light · Copper oxide · Interfacial charge transfer

1 Introduction

The global impact of the COVID-19 pandemic has been devastating, with over 7 million lives lost worldwide as of April 2024 [1, 2]. As COVID-19 continues to pose a recurrent and familiar public health threat, experts warn of the potential emergence of similar pandemics in the future [3, 4]. In response, healthcare authorities worldwide are proactively preparing for new pandemics, such as "Disease X" [5–7]. One key takeaway from the COVID-19 pandemic is the critical role of indirect transmission through contaminated surfaces and airborne droplets in the spread of SARS-CoV-2 [8–10]. Many commonly encountered

Yujin Lee, Kanghyun Lee and J.-unhyeop Shin contributed equally to this work.

✉ Tae Yong Kim
tykim11@koreatech.ac.kr

✉ Inho Nam
inhonam@cau.ac.kr

✉ Soomin Park
smpark@koreatech.ac.kr

[1] School of Energy, Materials and Chemical Engineering, Korea University of Technology and Education, Cheonan 31253, Republic of Korea

[2] Department of Chemical Engineering, Chung-Ang University, Seoul 06974, Republic of Korea

[3] Department of Advanced Materials Engineering, Chung-Ang University, Seoul 06974, Republic of Korea

[4] Department of Intelligent Energy and Industry, Chung-Ang University, Seoul 06974, Republic of Korea

[5] Department of Materials Science and Engineering, Research Institute of Advanced Materials, Seoul National University, Seoul 08826, Republic of Korea

Published online: 14 July 2025

surfaces in daily life, including silicone, plastic, and air filters, are composed of polymer matrices. Therefore, imparting long-term virucidal properties to these materials presents a promising strategy for mitigating virus transmission.

Copper (Cu) has attracted considerable attention due to its exceptional antimicrobial and antiviral properties [11–13]. Consequently, Cu-incorporated polymer matrices, such as antiviral films and coatings, are increasingly available in the market. In South Korea, for example, over five companies have commercialized Cu-containing antiviral polymer films, which are actively used in government offices and public spaces [14]. However, despite their widespread use, the long-term virucidal effectiveness of these materials remains unclear. Specifically, there is a lack of systematic studies on the Cu-based antiviral mechanism and the sustainability of Cu-containing polymer films, raising concerns about their reliability. Furthermore, challenges exist in scaling up their fabrication and ensuring long-term stability, particularly in maintaining the stability of Cu_xO ($x>1$) species over time.

The detailed mechanism by which Cu exerts its virucidal properties is not yet fully elucidated. However, it is known that the oxidation states of Cu play a pivotal role. It has been suggested that the virucidal mechanism of Cu involves the formation of a reactive oxygen species (ROS) [15], Cu ion leaching [16–18], and direct interaction between viruses and the oxidized Cu surface [19, 20]. Most studies agree that Cu(I), in the form of Cu_2O or partially reduced Cu_xO ($x>1$), exhibits strong virucidal activity due to its ability to adsorb and denature the protein. In contrast, CuO (Cu(II)) exhibits negligible virucidal activity [16, 21]. Previous efforts have attempted to develop Cu_2O-based coatings directly bound to the polymer surface [22]. However, Cu_2O is highly prone to self-oxidation, forming $Cu(OH)_2$ and eventually CuO, which lacks virucidal properties [16, 23]. Consequently, the antiviral activity of Cu_2O-containing materials deteriorates significantly over time under ambient and humid conditions, limiting their practical application in virucidal plastic and air filter products.

To address this limitation, we propose a method to impart long-term virucidal properties to commonly encountered surfaces such as silicone, plastics, and air filters. Our approach involves integrating Cu_xO-deposited TiO_2 (Cu_xO–TiO_2) nanoparticles into polymer matrices to sustain the virucidal activity of Cu species. In this Cu_xO–TiO_2 heterojunction system, electrons from the valence band (VB) of TiO_2 are directly transferred to Cu_xO under visible light irradiation via interfacial charge transfer (IFCT). Since the Cu(II)/Cu(I) redox potential ($E^0 = 0.16$ V vs. SHE, pH = 0) is more positive than the conduction band (CB) bottom of TiO_2 ($E^0 = -0.046$ V vs. SHE, pH = 0), visible light can initiate charge separation, promoting the IFCT from the VB of TiO_2 to Cu(II) in Cu_xO. This process maintains active Cu_xO ($x>1$) species, enabling the sustainable recovery of their virucidal effects.

While previous studies have explored Cu_xO–TiO_2 photocatalysts [21, 24–29], their focus has primarily been on antiviral performance, with limited understanding of the fundamental mechanisms that govern the regeneration of Cu_xO. Additionally, the application of Cu_xO–TiO_2 to commonly encountered surfaces, such as polymer films and plastics, remains unexplored, despite their critical importance for practical implementation. In this study, we demonstrate that not only Cu oxidation states but also the local atomic structure of Cu in specific Cu_xO-to-TiO_2 ratios significantly influences the optimal virucidal performance of Cu-containing surfaces. This finding contrasts with earlier studies that primarily attributed the antiviral effects of Cu_xO to its oxidation state alone, suggesting that the local atomic environment also plays a key role in enhancing virucidal activity in practical applications. We used X-ray absorption spectroscopy (XAS) to provide a theoretical explanation and establish a correlation between the Cu_xO–TiO_2 structure and its virucidal performance.

A common issue with adhesive-based surface coatings on polymer matrices is their susceptibility to mechanical stress, which can degrade long-term durability and weatherability [30, 31]. This issue can be addressed by blending Cu_xO–TiO_2 with molten polymers and additives. However, since virus inactivation primarily occurs at the surfaces of films and plastics rather than within the bulk, it is critical to strategically position Cu_xO–TiO_2 near the polymer surface to maximize its virucidal functionality. To achieve this, we exploit the surface segregation phenomenon of hydrophilic Cu_xO–TiO_2 nanoparticles in the hydrophobic molten state of polymeric media, as guided by deep learning–based molecular dynamics (MD) simulations. The preferential segregation of Cu_xO–TiO_2 toward the polymer surface is driven by thermodynamic stability, as hydrophilic nanoparticles tend to migrate to the surface in hydrophobic environments. MD simulations further demonstrate that this migration is energetically favorable due to Gibbs free energy minimization. This surface-specific positioning ensures efficient photocatalytic activation, exposure to visible light, and continuous Cu_xO regeneration—all critical factors for sustained virucidal functionality. Unlike conventional coatings, Cu_xO–TiO_2 is not merely adhered to the surface but is strategically integrated within a specific region of the polymer matrix, ensuring strong adhesion, mechanical stability, and long-term durability.

As a proof-of-concept study, we incorporate Cu_xO–TiO_2 into silicone, a widely used synthetic elastomer based on polydimethylsiloxane (PDMS) [32], and demonstrate a significant enhancement in virucidal performance against the model virus (bacteriophage Phi X 174). The silicone-integrated Cu_xO–TiO_2 film exhibited remarkable long-term

stability and structural robustness, retaining high virucidal activity even after extended exposure to ambient conditions. In both nanopowder and polymer composite forms, the virus inactivation kinetics are comparable to, or even superior to, those of previously reported Cu_xO–TiO_2-based photocatalysts (Table S1). To further broaden the applicability of our approach, we integrate Cu_xO–TiO_2 into both a polypropylene (PP) masterbatch and a nanofiber (NF) air filter, demonstrating its versatility and scalability across diverse material systems. The successful integration of Cu_xO–TiO_2 into polymer matrices using existing polymer processing techniques highlights its potential for mass production and commercialization. This advancement paves the way for large-scale deployment of durable, self-sanitizing materials in healthcare, public safety, and consumer applications, offering a practical and scalable solution for long-term virus mitigation.

2 Experimental section

2.1 Materials

All chemicals used were of reagent grade and employed without further purification. Titanium dioxide (TiO_2, rutile phase, 50 nm, Aladin), copper(I) bromide (CuBr, Sigma-Aldrich), and copper(II) chloride ($CuCl_2$, Sigma-Aldrich) were used as starting materials for the synthesis of Cu_xO–TiO_2 composites. Cu powder (Daejung) and a Cu-based polyethylene film (Intimo) were used as reference samples. The silicone elastomer base (SYLGARD 184, Dow Corning) was prepared in a 9:1 ratio with the curing agent. A PP homopolymer (H221P, SK Geo Centric) was utilized. Solutions for electrospinning were prepared using polyacrylonitrile (PAN) ($M_w = 150{,}000$, Sigma–Aldrich) and *N*, *N*-dimethylformamide (DMF, Daejung). Agar and a nutrient broth (BD Difco), along with PBS (pH 7.4, Sigma-Aldrich), were used for microbial culturing. All glassware and instruments were sterilized via autoclaving at 121 °C for 15 min before use.

2.2 Characterizations

The Cu content in the Cu_xO–TiO_2 samples was quantified using an inductively coupled plasma optical emission spectrometer (5100 ICP-OES, Agilent Technologies). HR-TEM (JEM-F200, JEOL), along with EDS (Dual SDD type, JEOL) and SEM (Apreo S HiVac, FEI), along with EDS (XFlash 6I100, BRUKER), were employed to analyze the surface morphology and elemental composition of the synthesized samples. The crystalline structure and diffuse reflectance were evaluated using XRD (EMPYREAN, PANalytical BV) and UV–Vis-NIR spectrophotometers (UV-3600i Plus, Shimadzu). The tensile and thermal properties of the polymeric specimens were assessed using a universal testing machine (NA-ST250K, Nanotech), a differential scanning calorimeter (Q20, TA Instruments), and a thermogravimetric analyzer (TGA 4000, PerkinElmer). The depth profiles of C 1 s, Si 1 s, O 1 s, and Ti 2p for Cu_xO–TiO_2-embedded PDMS (silicone) were obtained using X-ray photoelectron spectrometry (XPS, Thermo Scientific Nexsa) with a K-Alpha X-ray source. Depth profiling was performed using a monatomic Ar^+ ion gun for etching, conducted over 780 s at 5-s intervals with an X-ray spot size of 200 µm. TOF–SIMS was performed using an ION-TOF M6 instrument in positive polarity mode. A Bi^{3+} (30 kV) analysis gun with a raster size of 200×200 µm^2 was used for high-resolution surface characterization. Depth profiling was conducted using an Ar-cluster sputter gun (20 keV) over a 500×500 µm^2 area to examine the distribution of Ti^+ ions within the polymer matrix. X-ray absorption spectroscopy was performed at the 7D beamline of Pohang Light Source II (PLS-II) at Pohang Accelerator Laboratory. All Cu K-edge spectra were obtained in fluorescence mode using a 2.5-GeV storage ring with a ring current of 350 mA. XANES were processed using Athena software (ver. 0.9.26) for pre-edge, post-edge, background, and normalization. Fourier transformation of EXAFS (FT–EXAFS) data was performed using the Artemis software (ver. 0.9.26) with k^2 weight in the k-range of 1–13 Å^{-1} and in the R-range of 1.2–3.0 Å, for the FT–EXAFS fitting, the amplitude reduction factor ($S_0{}^2$), E_0 shift (ΔE_0), and interatomic distance (R) were fitted, while the Debye–Waller factor (σ^2) was fixed to prevent any negative σ^2 value. The obtained $S_0{}^2$ values of the scattering paths for the Cu_xO–TiO_2 samples were divided by the $S_0{}^2$ of the Cu foil reference sample to estimate the CN of the first-shell Cu–O and Cu–Cu bonds of the Cu_xO–TiO_2 samples. The WT–EXAFS spectra were obtained using WT–EXAFS software (https://github.com/Himmelspol/wtEXAFS). The $\chi(k)$ of a spectrum, exported using Athena software, was transformed using a Morlet wavelet with the parameters $\sigma = 1$ and $\eta = 10$.

2.3 Synthesis of Cu_xO–TiO_2

Cu_xO–TiO_2 composites were prepared via a wet impregnation method using TiO_2 nanoparticles as the host material (Fig. S1). A copper precursor (either CuBr or $CuCl_2$) was dissolved in a solvent system of either N, N-dimethylformamide (DMF, aprotic) or ethanol (protic) to form a homogeneous precursor solution. This solution was then mixed with TiO_2 using a planetary centrifugal mixer (ARM-310, THINKY). The Cu-to-TiO_2 ratio was adjusted by varying the concentration of the Cu precursor, while maintaining a fixed volume ratio of 3 mL of solution per 1 g of TiO_2. After impregnation, the slurry was dried overnight at 60 °C

to promote anchoring of Cu species on the TiO_2 surface. The dried composite was subsequently ground, washed with deionized water via centrifugation to remove unbound species, and vacuum-dried at 40 °C to yield the final Cu_xO–TiO_2 photocatalyst.

2.4 Preparation of Cu_xO–TiO_2-incorporated polymer matrices

To fabricate the Cu_xO–TiO_2-incorporated silicone samples, PDMS elastomer bases (SYLGARD 184, DOW) were homogeneously blended with varying amounts of Cu_xO–TiO_2 using a planetary centrifugal mixer (ARM–310, THINKY). Following the addition of a curing agent, the PDMS mixtures were degassed in a desiccator for 2 h and then cured overnight at 60 °C in an oven. For the Cu_xO–TiO_2-incorporated PP samples, a conventional extrusion and injection molding process was employed. The mixture of PP and Cu_xO–TiO_2 was processed using a co–rotating twin screw extruder (Bautek BA19, $D = 19$ mm, $L/D = 40$, South Korea) at 150–180 °C with a rotor speed of 50 rpm. The resulting Cu_xO–TiO_2-incorporated PP masterbatch was then injection-molded using an Arburg injection molding machine (Allrounder 320c, GINDUMAC) to produce dog bone-shaped specimens, conforming to the dimensions specified in the ISO 527–2 standard for tensile testing.

2.5 Preparation of Cu_xO–TiO_2-incorporated NFs

A solution was prepared by dissolving 1 g of PAN and 1 g of synthesized Cu_xO–TiO_2 in 9 g of DMF. This mixture was stirred magnetically at 300 rpm at room temperature for 1 h. The solution was then loaded into a 10-mL syringe equipped with a stainless-steel tip (Φ 0.6 × L 26 mm). A nonwoven fabric (20 × 30 cm^2) was secured to the rotating cylinder collector of the electrospinning apparatus (ESR200RD, Nano NC). The syringe was mounted onto the apparatus, and electrospinning was performed at a distance of 10 cm with a voltage setting of 8.4 kV, rotation speed of 150 rpm, and flow rate of 0.2 mL h^{-1}. After 10 h, 2 mL of the solution was electrospun to produce the NF filter.

2.6 Culture of Phi X 174 and inactivation experiment

The population of bacteriophage Phi X 174 was quantified using a plaque assay, utilizing *Escherichia coli* (ATCC 13706) as the host bacterium. The phages were separated from the culture media by centrifuging three times at 3000 × *g* for 15 min. For culturing, agar plates mixed with a nutrient broth were prepared, stored at 4 °C, and then pre-warmed to 37 °C for 30 min before experimentation. Visible light illumination was conducted using a 100-W xenon lamp (LCS-100, ORIEL) equipped with AM1.5G and a long-pass filter ($\lambda > 400$ nm), producing an irradiation power of 80 mW cm^{-2}. To assess the virucidal activity of the Cu_xO–TiO_2 nanopowder, 0.033 g of Cu_xO–TiO_2 was placed on Petri dishes (35 × 10 mm) and topped with 3 mL of a virus solution initially containing 10^7–10^8 PFU mL^{-1}. The samples were exposed to both light and dark conditions with stirring. At predefined time intervals, 0.1 mL of the virus solutions was collected, serially diluted in PBS, and then analyzed using a plaque assay to count the viral particles [17, 27]. The viral inactivation efficacy was further evaluated using a modified ISO 22196 method on both silicone and electrospun NF filters. For silicone samples, after 30 min of pre-illumination, 0.5 mL of virus solution was applied to the PDMS surface, covered with a polyvinyl chloride (PVC) film to prevent evaporation. For NF filters, 3 mL of the virus solution was deposited onto a 4 × 4 cm^2 section for testing. The solutions from both materials were immediately processed for viral activity assessment by serial dilutions and plaque assays.

2.7 MD simulation

For all calculations, deep learning-based simulations were conducted using the universal neural network potential (PFP version 4.0.0) implemented in Matlantis (Preferred Computational Chemistry, Inc.). The Atomic Simulation Environment (ASE) functions, written in Python, were utilized. The TiO_2-incorporated PDMS structure was simulated by first optimizing the PDMS structure comprising nine monomers and the TiO_2 structure using the limited-memory Broyden–Fletcher–Goldfarb–Shanno (L-BFGS) algorithm. To incorporate 10 wt.% TiO_2 into PDMS, the structure was initially formed using Packmol software, and structural optimization was conducted. The reliability of the optimized structure was ensured through MD simulations using the NPT ensemble until the volume change converged at 300 K and 100 kPa pressure. To verify the aggregation, the structure was subjected to MD simulations in an NVT ensemble for 140 ps at 300 K. Additionally, a vacuum (40 Å) was created above the bulk structure to form a slab structure for surface simulations, which were then subjected to MD simulations using the NVT ensemble at 300 K to confirm temperature-dependent segregation and aggregation.

3 Results and discussion

3.1 Characterizations of Cu_xO–TiO_2

Figure 1a illustrates the IFCT mechanism between Cu_xO and TiO_2, leading to the virucidal activity of Cu_xO–TiO_2 materials. Under visible light irradiation ($\lambda > 400$ nm), electrons

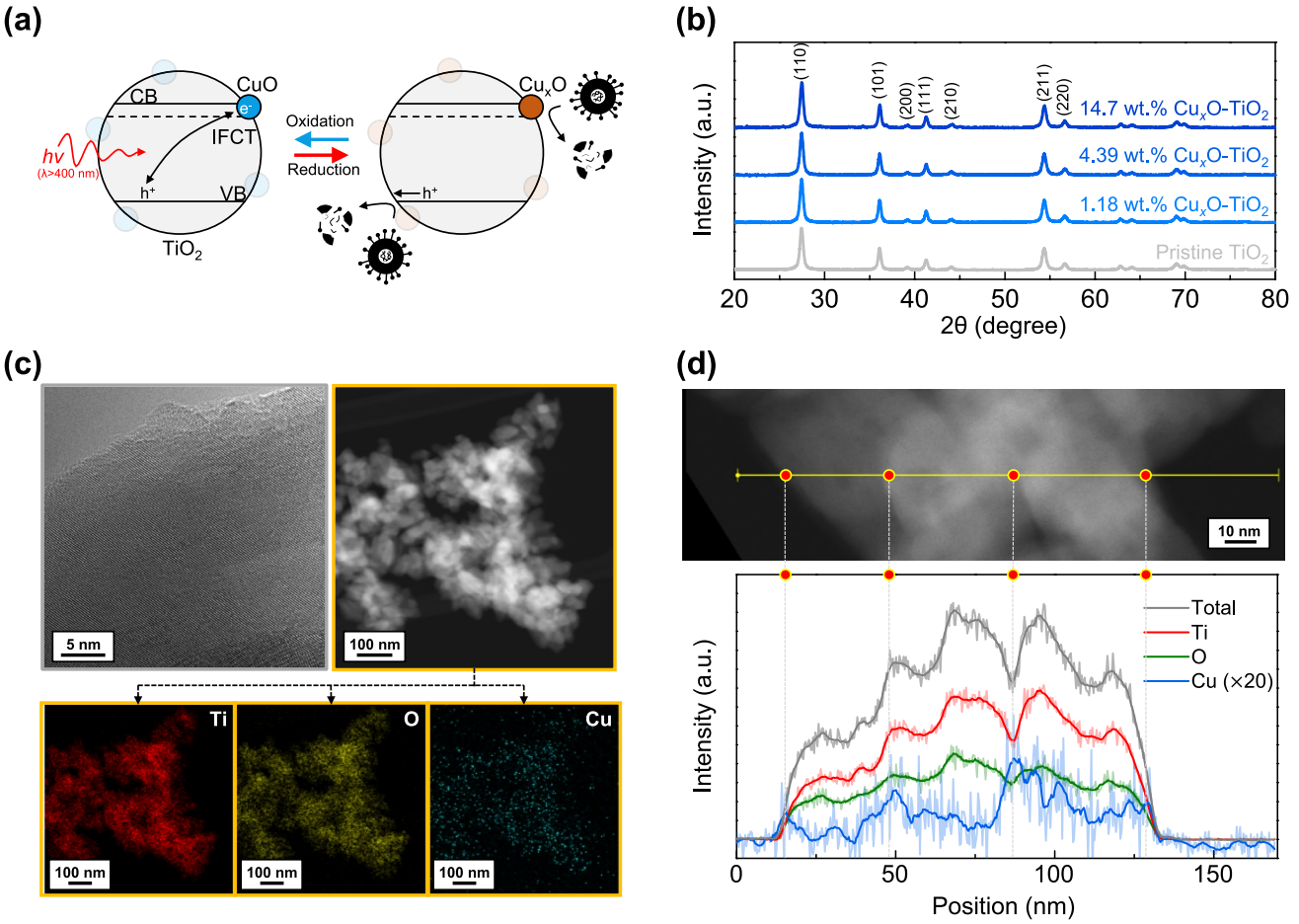

Fig. 1 Characterizations of synthesized Cu_xO–TiO_2 materials. **a** Schematic illustration of the interfacial charge transfer and virucidal mechanisms of Cu_xO–TiO_2 under visible light irradiation. **b** XRD patterns of Cu_xO–TiO_2 with various loading amounts of Cu_xO. **c** Bright and dark field HR-TEM images of Cu_xO–TiO_2, along with elemental mapping results for Ti, O, and Cu. **d** Results of TEM-EDS line scan analysis, showing Ti, O, and Cu elemental intensity profiles plotted as a function of scan distance. Marked positions denote areas between Cu_xO–TiO_2 particles

and holes are generated, with electrons being captured by the CuO grafted on the TiO_2 surface due to the more positive potential of the Cu(II)/Cu(I) redox couple compared to the TiO_2 CB [33, 34]. This process results in the formation of partially reduced Cu_xO ($x > 1$), which exhibits potent virucidal activity. The Cu_xO–TiO_2 materials were synthesized by wet-impregnation of Cu precursor at varying concentrations onto rutile-phase commercial TiO_2 particles. Cu loading was determined by inductively coupled plasma-optical emission spectroscopy (ICP–OES). X-ray diffraction (XRD) data in Fig. 1b show the main XRD peaks corresponding to rutile TiO_2 phases (110), (101), (111), and (211) [35, 36], with no detectable peaks for CuO or Cu_2O, regardless of Cu_xO loading. This suggests that the grafted Cu_xO exists as amorphous atomic clusters or ionic species.

Figure 1c shows bright- and dark-field high-resolution transmission electron microscopy (HR-TEM) and energy-dispersive X-ray spectroscopy (EDS) analysis of the Cu_xO–TiO_2 materials. Rutile TiO_2, with an average particle size of approximately 50 nm, was observed, but no distinct Cu_xO crystals were detected, consistent with the XRD results indicating the amorphous nature of Cu_xO. EDS elemental mapping for Ti, O, and Cu revealed a uniform distribution of Cu on TiO_2, suggesting a high dispersion of sub-nano-Cu_xO. Further TEM–EDS line scan analysis (Fig. 1d) showed higher Cu intensities on the TiO_2 surface, confirming the successful grafting of Cu_xO onto the surface rather than in the bulk. The finely distributed Cu_xO clusters on the TiO_2 surface are expected to enhance IFCT following visible-light-induced charge separation [37].

3.2 Mechanistic study on virucidal efficacy of Cu_xO–TiO_2

To evaluate the virucidal activity of Cu_xO–TiO_2 materials, Phi X 174 bacteriophage was used, and the virus titer was

quantified using the plaque assay method [18, 28]. Figure 2a compares the virucidal performance of Cu_xO–TiO_2 (4.39 wt.% of Cu loading) to that of pristine TiO_2 under both dark and visible light irradiation. The optimal Cu loading for maximizing the normalized inactivation rate constant for Phi X 174 was determined to be 4.39 wt.%, as discussed below. After a 5-min dark period for virus absorption, visible light irradiation was applied, leading to rapid virus inactivation. This resulted in an 8.67-ln reduction within just 3 min, demonstrating competitive virucidal efficacy compared to previously reported nanopowder materials, even under lower light intensities and significantly shorter exposure times (Table S1). These findings validate the successful operation of the photoinduced IFCT-mediated virucidal mechanism outlined in Fig. 1a. In contrast, no significant inactivation was observed under other conditions, including Cu_xO–TiO_2 without light irradiation and pristine TiO_2 under both light and dark conditions. The virus inactivation kinetics were analyzed using the pseudo-first-order rate equation, yielding an inactivation rate constant of 131 h^{-1} for Cu_xO–TiO_2 under visible light (Fig. 2b). For other conditions, the inactivation rate constant was less than 3.92 h^{-1}.

Figure 2c presents diffused reflectance spectroscopy (DRS) data comparing Cu_xO–TiO_2 with pristine TiO_2. Cu_xO–TiO_2 exhibited significantly enhanced absorption in the visible light range, with increased absorption in the 400–500 nm range attributed to IFCT between TiO_2 and Cu_xO, and absorption in the 550–900 nm range due to the 1.7-eV bandgap of CuO [38]. To assess wavelength-dependent virucidal activity, we used optical filters that selectively cut off various wavelength ranges while maintaining consistent light intensity. The inset of Fig. 2c shows a clear

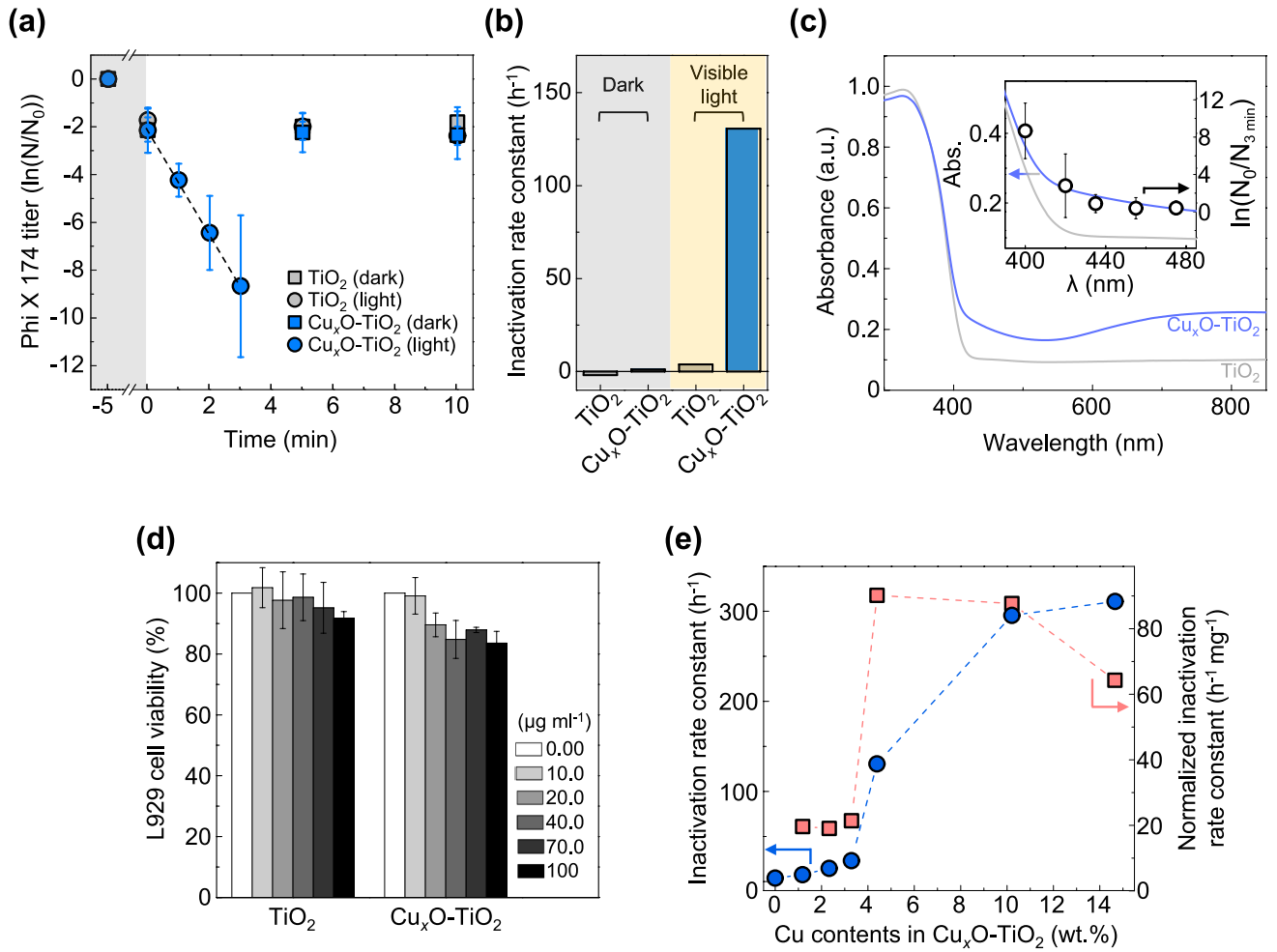

Fig. 2 Virucidal activities of Cu_xO–TiO_2 materials. **a** Inactivation kinetics of Phi X 174 by TiO_2 and Cu_xO–TiO_2 under dark and visible light conditions. **b** Inactivation rate constants under various conditions calculated using the pseudo-first-order equation. **c** DRS spectra comparing Cu_xO–TiO_2 and pristine TiO_2. Inset: Correlation with wavelength-dependent virucidal activities. **d** Cell viability of L929 fibroblasts after exposure to Cu_xO–TiO_2 and pristine TiO_2 at various concentrations up to 100 μg $m.^{-1}$, determined by MTT assay. **e** Change in inactivation rate constants and normalized inactivation rate constants based on incorporated Cu weights with increasing Cu content in Cu_xO–TiO_2

correlation between the absorption spectrum of Cu_xO–TiO_2 and the wavelength-dependent virucidal activity, further confirming the efficacy of visible-light-driven virucidal mechanisms in these materials. To ensure the seamless integration of virucidal Cu_xO–TiO_2 into everyday polymer products, it is essential to confirm that it does not exhibit significant cytotoxicity to mammalian cells. To assess non-toxicity, L929 fibroblastic cell lines were exposed to increasing concentrations of Cu_xO–TiO_2 for 24 h, followed by a 3-(4,5-dimethylthiazole-2-yl)−2,5-diphenyltetrazolium bromide (MTT) assay [39]. As shown in Fig. 2d, cell viability was approximately 99.1% at a concentration of 10 μg mL^{-1} after 24 h of incubation. At 100 μg mL^{-1}, the viability slightly decreased to 83.4 ± 3.87%. In comparison, pristine TiO_2, considered safe by the US Food and Drug Administration (FDA) [40, 41], exhibited a cell viability of 91.7 ± 2.16% at 100 μg mL^{-1}. The minimal difference in cell viability between TiO_2 and Cu_xO–TiO_2 suggests that virucidal Cu_xO–TiO_2 does not exhibit significant cytotoxicity.

To evaluate the impact of Cu loading on the photocatalytic virucidal efficacy of Cu_xO–TiO_2, we measured the inactivation rate constants of Cu_xO–TiO_2 at varying Cu concentrations (Fig. 2e). If the amount of active Cu(I) is the primary factor in the virucidal activity, the inactivation rate constants should show a linear or log-linear correlation with Cu content in Cu_xO–TiO_2. Based on this, higher Cu contents would likely lead to low or consistent normalized (by Cu content) inactivation rate constants due to the relative abundance of TiO_2 per unit Cu_xO. This was observed for samples with 1.18 and 2.33 wt.% Cu loading on TiO_2. However, contrary to this expectation, the normalized inactivation rate constants significantly increased when Cu content exceeded 4.39 wt.%, along with a rapid rise in the inactivation rate constants. This suggests that virucidal performance is influenced not only by the Cu_xO quantity (which needs to exceed 4.39 wt.%) but also by the specific atomic structure at higher Cu_xO concentrations. Therefore, it is likely that different chemical states contribute to the exceptional virucidal activity of Cu_xO–TiO_2 [16]. Notably, only 0.12% of Cu leached from Cu_xO–TiO_2 in phosphate-buffered saline (PBS), indicating negligible leaching and confirming the high stability of the Cu_xO active sites, regardless of Cu loading (Fig. S2).

To investigate how the distinct Cu species in Cu_xO–TiO_2 influence its virucidal performance, we conducted X-ray absorption near-edge structure (XANES) and extended X-ray absorption fine structure (EXAFS) analyses on Cu_xO–TiO_2 samples with varying Cu loadings (1.18, 2.33, 4.39, 10.2, and 14.7 wt.%). The XANES spectra are shown in Fig. 3a. No pre-edge features indicative of Cu_2O (8982 eV) or metallic Cu (8981 eV) were observed, ruling out the presence of Cu(I) or Cu(0) in the dark state. The absorption edge for Cu_xO–TiO_2 with 1.18 wt.% Cu shifted to a higher energy level than that of the CuO reference, and its white line intensity (around 9000 eV) was greater, indicating that Cu atoms in this sample are highly coordinated with O atoms and have a coordination number (CN) greater than the CuO reference (CN = 4). When Cu content exceeded 4.39 wt.%, the absorption edge shifted to a lower energy level, approaching that of the CuO reference in the 10.2 and 14.7 wt.% Cu_xO–TiO_2 samples. The absorption edge energy and white line intensity correlated with the Cu oxidation state and CN with O atoms, respectively (Fig. S3) [33, 42, 43]. This suggests that Cu_xO–TiO_2 with > 4.39 wt.% Cu exhibits a lower Cu oxidation state and a lower CN with O atoms.

The wavelet-transformed EXAFS (WT–EXAFS) spectra are shown in Fig. 3b. Fourier-transformed EXAFS (FT–EXAFS) and first-shell fitting results are provided in the Supplementary Information (Fig. S4 and Table S2). Cu → O scattering paths at approximately 1.5 Å in *R*-space were observed for all Cu_xO–TiO_2 samples. Notably, *k*-space oscillations between 2 and 10 $Å^{-1}$ correspond to these scattering paths. The second-shell Cu → (–O–)Cu scattering at 2.9–3.0 Å was observed for all Cu_xO–TiO_2 samples, indicating the formation of Cu_xO clusters. A key observation is that the magnitude of Cu → O paths decreases with increasing Cu content, suggesting a lower CN of Cu–O bonds in samples with higher Cu content, in agreement with the XANES spectra. Cu → Cu scattering paths at approximately 2.1 Å were observed in the 4.39, 10.2, and 14.7 wt.% Cu_xO–TiO_2 samples, with *k*–space oscillations between 6 and 10 $Å^{-1}$, indicating the absence of Cu–metal bonds such as Cu–Ti bonds.

The CNs for the first-shell Cu–O and Cu–Cu bonds, estimated from fitting the FT–EXAFS spectra, are shown in Fig. 3c. For Cu_xO–TiO_2 with 1.18 wt.% Cu, the Cu–O CN is approximately 6, typical for the maximum coordination of 3 d transition metals. However, as the Cu content increases beyond 4.39 wt.%, the Cu–O CN decreases to around 3, even smaller than that for CuO (CN = 4). This suggests that Cu_xO clusters are partially reduced to Cu_2O–like structures (CN = 2). EXAFS results show Cu–Cu bonds in samples with higher Cu content, but XANES data indicate no metallic Cu(0) species formation (no pre-edge peak for Cu(0)). Therefore, the Cu–Cu in Cu_xO–TiO_2 (with ≥ 4.39 wt.% Cu) are likely isolated bonds in distorted, amorphous Cu_xO species, associated with a low Cu–O CN.

CuO species with a high Cu–O CN (> 4) are predominant in Cu_xO–TiO_2 at low Cu loadings, whereas at Cu contents ≥ 4.39 wt.%, a structural shift occurs toward Cu_xO clusters featuring lower Cu–O CN (~ 3) and the emergence of Cu–Cu coordination (Fig. 3d). This transition, observed in X-ray absorption spectroscopy, correlates with the sharp enhancement in virucidal activity results (Fig. 2e), suggesting that lower Cu–O CN and the formation of Cu–Cu domains plays a critical role in facilitating photocatalytic

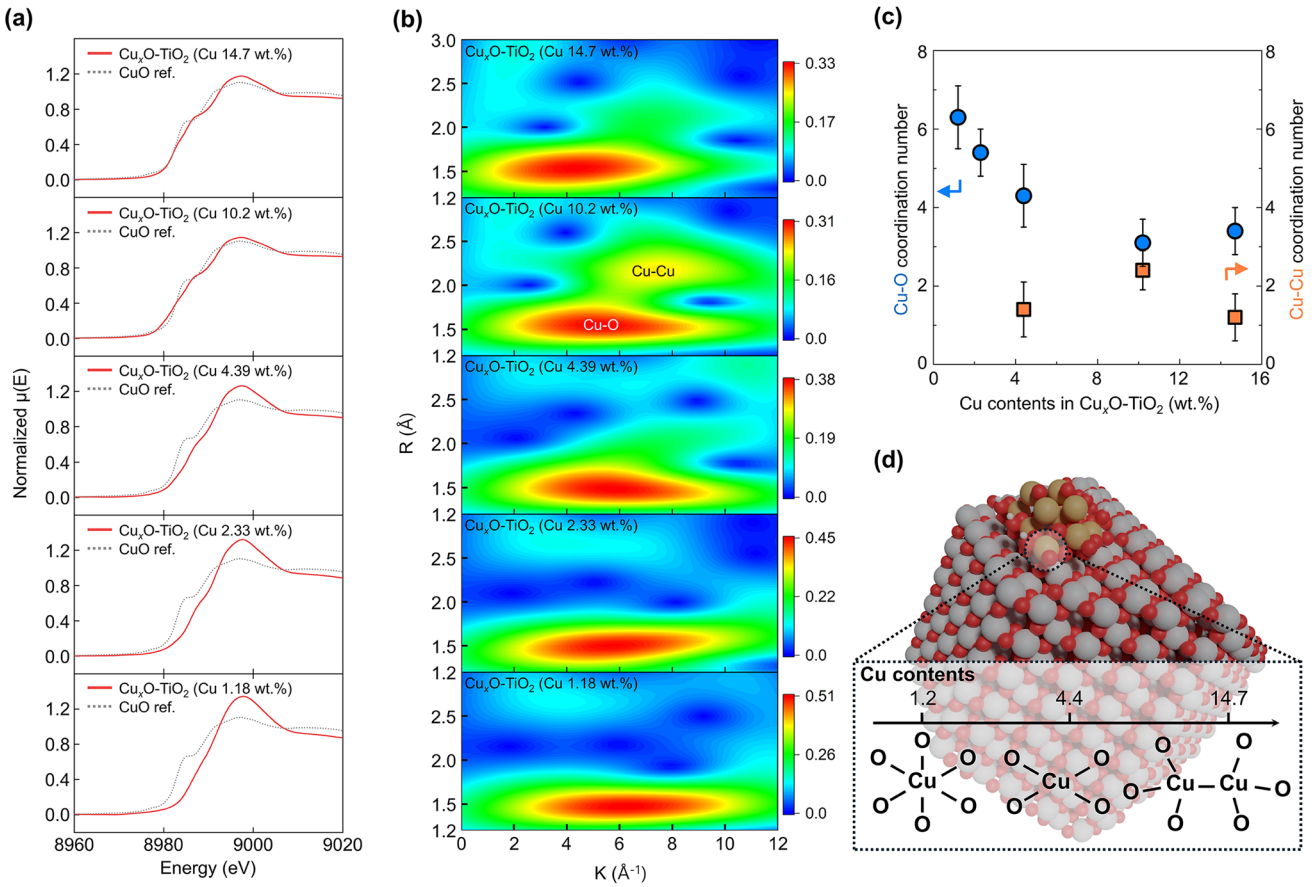

Fig. 3 X-ray absorption investigations of Cu species in Cu_xO–TiO_2 materials. **a** XANES spectra of Cu_xO–TiO_2 with varying Cu loading amounts. **b** WT-EXAFS spectra of Cu_xO–TiO_2 with different Cu contents. **c** Quantified coordination numbers (CN) for Cu–O and Cu–Cu bonds, estimated from fitting the FT-EXAFS spectra. **d** Proposed structural differences of Cu_xO species on TiO_2

IFCT to Cu_xO. This is likely due to the increased structural similarity to reduced species and the improved charge-accepting ability of Cu–Cu clusters.

To further substantiate this interpretation, we analyzed DRS spectra and their first derivatives ($-\mathrm{d}A/\mathrm{d}\lambda$), which revealed a distinct increase in visible-light absorption above 4.39 wt.% Cu—coinciding precisely with the onset of Cu–Cu coordination (Fig. S5). These optical features provide additional evidence that Cu–Cu cluster formation enhances IFCT efficiency. To examine how this structural motif influences virucidal activity at the molecular level, we performed atomistic simulations using a machine learning potential. The adsorption and dissociation of an arginine-glycine dipeptide—a motif from bacteriophage capsid protein [44]—were modeled on Cu_xO–TiO_2 surfaces featuring either isolated Cu–O or aggregated Cu–Cu coordination (Fig. S6). The calculated reaction energy profiles indicate that Cu–Cu–rich surfaces enable stronger peptide binding and more exergonic bond cleavage, suggesting a more favorable pathway for capsid degradation. Taken together, these results establish a mechanistic link between local Cu coordination, IFCT enhancement, and viral protein decomposition, elucidating how Cu–Cu interactions within Cu_xO contribute directly to the sustained antiviral performance of the composite.

3.3 Incorporation of Cu_xO–TiO_2 into silicone

To maximize the virucidal effectiveness of polymer matrices, it is crucial to position the Cu_xO–TiO_2 near the surface to facilitate interaction with viruses from environmental or human sources. Additionally, managing nanoparticle aggregation is essential, as uncontrolled dispersion could lead to inhalation risks. Nano–sized particles can become airborne and potentially pose health hazards [45]. To overcome these challenges, we propose two strategies to ensure that Cu_xO–TiO_2 particles are stably located near the surface of polymer matrices, thereby improving antiviral efficacy. As a proof-of-concept, we incorporate Cu_xO–TiO_2 into silicone, a widely used synthetic elastomer based on polydimethylsiloxane (PDMS) [32].

The first strategy involves promoting surface segregation between silicone and Cu_xO–TiO_2. After thorough mixing in the hydrophobic bulk, scanning electron microscopy (SEM) images and corresponding EDS elemental mappings for Si and Ti (Fig. 4a–f) reveal that Cu_xO–TiO_2 particles are effectively localized near the surface of the cured silicone polymer. To validate these findings, we employed time-of-flight secondary ion mass spectrometry (TOF–SIMS) analysis and X-ray photoelectron spectroscopy (XPS) depth profiling, which provides high surface sensitivity, to accurately assess the spatial distribution of TiO_2 within the silicone matrix (Fig. 4g, h).

TOF–SIMS analysis confirms that TiO_2 is primarily localized near the surface rather than being uniformly distributed throughout the bulk material (Fig. 4g). The intensity of Ti peaks is highest just beneath the surface and decreases gradually with depth, indicating a depth-dependent distribution of TiO_2. This surface-localized arrangement suggests that Cu_xO–TiO_2 particles are concentrated within the surface region of the silicone layer, which helps maintain the antiviral activity of Cu_xO by facilitating charge transfer and minimizing excessive oxidation. Further confirmation of this surface positioning comes from XPS depth profiling (Fig. 4h), which shows that the Ti 2p signal is detectable within 20 s of sputtering. Given that the typical etch rate for XPS depth profiling of 10^{-2}–10^{-1} nm s^{-1} [46–48], this result indicates that the top of the Cu_xO–TiO_2 cluster is positioned within the polymer at a depth of no more than a sub-nanometer from the surface.

MD simulations, conducted in the nVT ensemble with the deep learning–based potential (Fig. 4i and j; Supplementary Video S1), demonstrated that TiO_2 particles migrate from the bulk to the surface. This migration of TiO_2 particles is driven by a tendency to minimize Gibbs free energy for thermodynamic stability, as confirmed by energy calculations showing stabilization from − 11,387 to − 11,418 eV. This phenomenon is evidenced by the low surface energy of Cu_xO–TiO_2, which facilitates surface migration [49, 50]. Such behavior is consistent with previous studies that showed that hydrophilic particles migrate to the surface in hydrophobic environments [51].

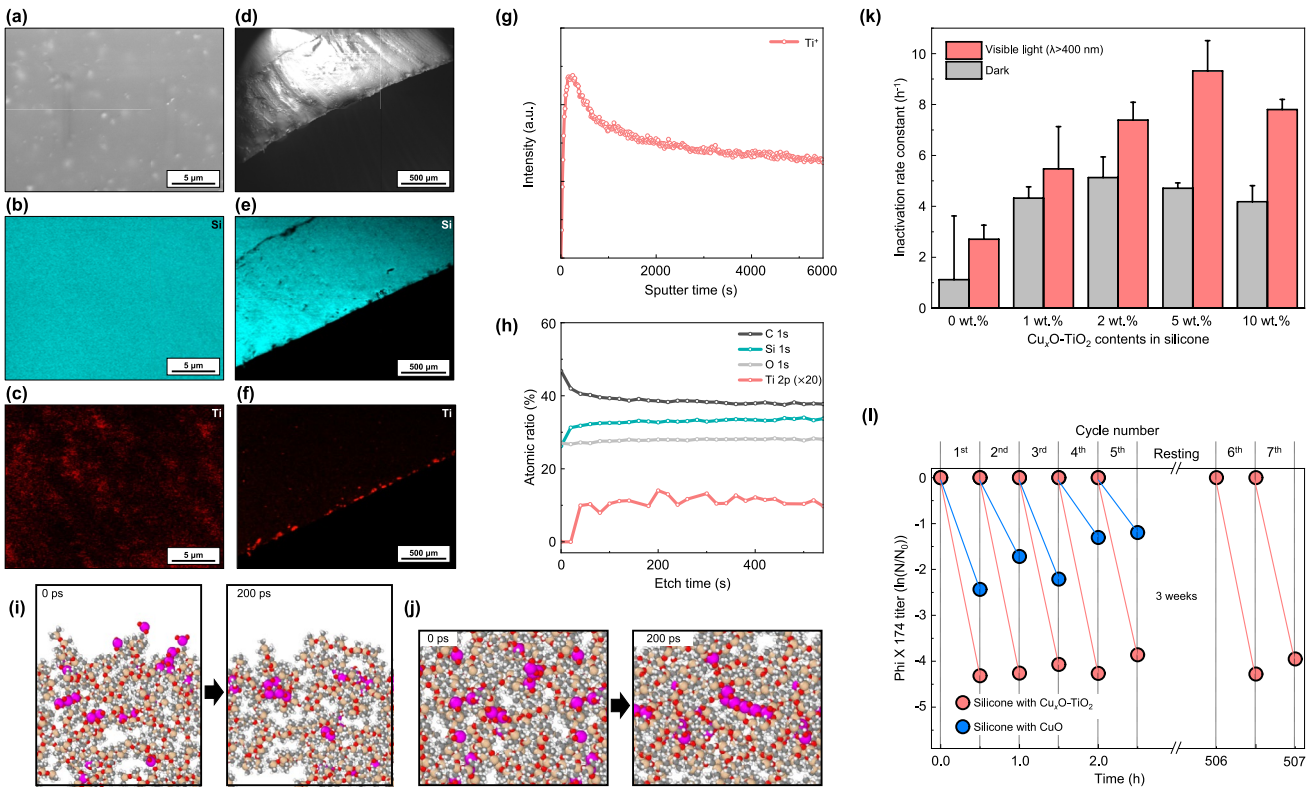

Fig. 4 Properties of Cu_xO–TiO_2-embedded silicone. **a** Top-view and **d** side-view SEM images, with **b**, **c**, **e**, and **f** corresponding EDS elemental mappings showing the distribution of Si and Ti. **g** TOF–SIMS depth profile of Ti^+ secondary ion signal, illustrating their distribution within the silicone matrix. **h** XPS depth profile of Cu_xO–TiO_2-embedded silicone, displaying the atomic ratios of C, Si, O, and Ti across different etching times. **i** Side view and **j** top view of MD simulation results of a slab structure over 200 ps at 300 K. Atoms are colored as follows: pink for Ti, red for O, white for H, light brown for Si, and gray for C. **k** Inactivation rate constants of virucidal silicone with varying Cu_xO–TiO_2 contents. **l** Repeated inactivation of bacteriophage Phi X 174 by silicone embedded with 5 wt.% Cu_xO–TiO_2 under visible light, compared to silicone with an equivalent amount of pure Cu powder

The second method involves the aggregation of Cu_xO–TiO_2 particles that migrate to the surface due to segregation and then accumulate in a confined two-dimensional space. This reduces the distance between particles, initiating granulation. To explain this aggregation phenomenon, we applied the extended Derjaguin–Landau–Verwey–Overbeek (DLVO) theory and the polymeric barrier potential, a repulsive force within polymer matrices like silicone [52]. The extended DLVO theory accounts for nanoparticle coagulation and dispersion in polymer matrices through van der Waals attraction, electrostatic repulsion, and polymeric barrier potential, as shown in Eq. (1) [53].

$$V_{total}(r) = -\frac{A_{TiO_2\cdot\text{silicone}}}{6}\left(\frac{2a^2}{r^2-4a^2} + \frac{2a^2}{r^2} + ln\left(\frac{r^2-4a^2}{r^2}\right)\right) + \frac{64\pi k_B T a \rho_\infty}{\kappa^2}\tanh^2\left(\frac{ze\zeta}{4k_B T}\right)\exp(-\kappa r) + 4\pi\epsilon a^2\sigma \quad (1)$$

Equation (1) is detailed in Supplementary Note S1. Cu_xO–TiO_2 exhibits a high Hamaker constant in the silicone matrix, indicating stronger van der Waals attraction [54]. Conversely, the low dielectric constant of silicone (30 times lower than that of water) and its low surface potential reduce electrostatic repulsion, making van der Waals forces dominant in the DLVO framework [55].

Due to the reduced role of electrostatic forces, the polymeric barrier potential becomes the primary repulsive force within polymer matrices. This potential is influenced by particle size, a grafting ratio of the linear polymer, and the interaction parameter [56]. As segregation brings primary Cu_xO–TiO_2 particles closer together within silicone, the small particle size weakens the polymeric repulsion. Consequently, van der Waals interactions dominate, leading to particle aggregation even at low concentrations and the formation of secondary particles around 1 μm in diameter (Fig. S7). This aggregation behavior was also observed in the MD simulations. Initially, TiO_2 particles were distributed sporadically, but over time, they aggregated to form secondary particles, eventually forming two distinct clusters at 140 ps (Fig. S8 and Supplementary Video S2).

Secondary particles can be observed on the silicone surface at 1, 2, and 5 wt.% of Cu_xO–TiO_2 (Fig. S9). At 10 wt.% Cu_xO–TiO_2, tertiary particles of approximately 5 μm in diameter form (Fig. S10). The formation of these large tertiary particles significantly reduces the virucidal performance of the silicone, as discussed below. Unlike the smaller primary particles, the secondary particles (~ 1 μm) experience stronger polymeric repulsion due to the silicone matrix. The interparticle distances for concentrations of 1, 2, and 5 wt.% are 3.11, 2.38, and 1.46 μm, respectively, aligning with the expected trend for a two-dimensional spatial arrangement (Fig. S11). Based on this trend, the interparticle distance at 10 wt.% is predicted to be 0.98 μm. Interaction force calculation shows that for distances greater than 1.2 μm, repulsion due to grafted silicone dominates, particularly with the large secondary particles (Fig. S12). Below 1.2 μm, van der Waals attraction becomes the predominant force, overcoming the polymeric repulsion at the predicted interparticle distances for 10 wt.%, leading to the formation of tertiary particles over 5 μm (see Supplementary Note S1 for detailed calculations). These results indicate that the interplay between segregation and aggregation of Cu_xO–TiO_2 particles within the silicone matrix contributes to optimal antiviral performance.

The virucidal activities of Cu_xO–TiO_2-embedded silicone were evaluated using a modified ISO 22196:2011 method, which involved sequential inoculation, film adhesion, incubation, and plaque assay quantification [57]. The incubation was carried out for 30 min under both dark and visible light conditions at ambient temperature. Silicone samples containing 0, 1, 2, 5, and 10 wt.% Cu_xO–TiO_2 were prepared, with Cu_xO–TiO_2 nanoparticles (4.39 wt.% Cu) blended into the PDMS base. All samples were pre-illuminated with visible light for 30 min to generate Cu(I) species before testing. The inactivation kinetics of Phi X 174 were analyzed using the pseudo-first-order rate equation, yielding inactivation rate constants shown in Fig. 4k. Under dark conditions, silicone with Cu_xO–TiO_2 exhibited higher inactivation rates (4–5 h^{-1}) compared to pure silicone (0 wt.%), which had a rate of 1.12 h^{-1}. This enhancement in virucidal activity is likely due to the pre-formed Cu(I) species resulting from the pre–illumination. Furthermore, studies on light intensity and wavelength dependence confirmed that the composite responds most effectively to strong visible light, particularly in the 400–500 nm, consistent with the IFCT-driven activation mechanisms (Figs. 2c, S13, and S14).

Virucidal activities were significantly enhanced under visible light, with the highest rate reaching 9.32 h^{-1} at 5 wt.% Cu_xO–TiO_2, demonstrating superior performance compared to dark conditions at equivalent concentrations. This increase is attributed to the critical role of IFCT in the embedded Cu_xO–TiO_2 particles upon light irradiation. However, at higher Cu_xO–TiO_2 concentrations, virucidal performance decreased, likely due to the formation of tertiary particles in the hydrophobic silicone matrix. SEM and EDS data for silicone polymers with higher Cu_xO–TiO_2 concentrations show significant aggregation of particles within the matrix (Fig. S10) and a subsequent reduction in their tensile properties (Fig. S15 and Table S3), indicating that hydrophilic Cu_xO–TiO_2 particles aggregate rather than disperse at high concentrations.

This non–linear performance trend is consistent with previous studies that have reported the dual role of nanoparticle aggregation in photocatalytic systems. Specifically, moderate clustering has been shown to promote charge transfer and enhance interfacial activity, thereby improving photocatalytic efficiency [58–61]. In contrast, excessive aggregation leads to adverse effects such as light scattering and reduced

surface accessibility, ultimately impairing overall reactivity [62–64]. The behavior observed in our silicone–based composite system aligns with this broader understanding and highlights the importance of modulating interparticle interactions in solid-state matrices to optimize photocatalytic and virucidal performance.

To evaluate the sustainability of virucidal performance, viral inactivation tests were conducted on silicone composites containing 5 wt.% of Cu_xO–TiO_2, which exhibited the highest initial activity. Repeated inoculations were performed under visible light (Fig. 4l). In the first cycle, the silicone sample achieved a 4.32-ln reduction in viral activity after 30 min. By the fifth cycle, the reduction decreased to 3.86 ln (89.4% of the initial performance), with minimal loss of activity. After resting for 3 weeks at ambient temperature and humidity, a subsequent test showed a 4.28-ln reduction (99.1% of the initial performance), and the activity remained stable, maintaining 91.6% of its original effectiveness. To further evaluate the robustness against environmental and mechanical stresses, supplementary experiments were carried out under high humidity (99% RH), varying storage temperatures (4, 20, and 40 °C), and simulated surface abrasion. As shown in Fig. S16, the composite maintained high virucidal activity across all conditions, with temporary fluctuations attributable to environmental modulation of viral stability rather than any functional degradation of the material. Notably, virucidal activity consistently recovered under ambient conditions, confirming the robustness and resilience of the Cu_xO–TiO_2-embedded silicone composite against environmental variation. Additionally, in simulated abrasion tests mimicking repeated physical contact, the composite retained stable virucidal performance up to a 1.67 wt.% weight loss (Fig. S17).

In parallel, an acute ecotoxicological assessment using *Daphnia magna* showed no observable toxicity for pristine, TiO_2-embedded, or Cu_xO–TiO_2-embedded silicone composites. This confirms that the incorporation of Cu_xO–TiO_2 does not induce acute aquatic toxicity and supports the environmental safety of the material under the tested conditions (Table S4). The absence of toxicity is likely due to the minimal release of Cu ions from the embedded photocatalyst, previously verified through ion-leaching analysis (Fig. S2), as well as the robust confinement of Cu_xO–TiO_2 particles near the polymer surface.

This sustained performance highlights the successful IFCT between Cu_xO and TiO_2, despite the inherent instability of Cu(I), which typically oxidizes to Cu(II), a non-virucidal form. In contrast, silicone composites containing only Cu_xO (without TiO_2) showed significantly lower initial activity (2.44-ln reduction) and poor sustainability, with only a 1.20-ln reduction in the fifth cycle, close to natural decay under the same conditions. A control experiment using a commercially available Cu-containing polyethylene film demonstrated negligible virucidal performance, further indicating rapid oxidation of Cu on the film (Fig. S18) [16, 28].

Table S1 presents a comparative analysis of the virucidal performance of Cu_xO–TiO_2 in both nanopowder and polymer composite forms [28, 65–67]. Furthermore, additional comparisons were made under identical conditions with representative anti–microbial and virucidal materials such as Ag, Fe_3O_4, ZnO, and WO_3, as shown in Fig. S19 [68–71]. The superior inactivation rate of the Cu_xO–TiO_2 nanopowder developed in this study, combined with its strategic incorporation into polymer matrices, results in remarkable long-term stability and structural robustness. This approach maintains high virucidal activity even after prolonged exposure to ambient conditions—an advantage not observed in previous systems, where particle aggregation, reduced stability, and diminished activity over time pose significant challenges. These findings emphasize the distinct benefits of integrating Cu_xO–TiO_2 into polymer matrices, providing improved durability, scalability, and practicality for real-world applications.

To demonstrate the large-scale producibility of this strategy, we incorporated Cu_xO–TiO_2 nanoparticles into the mixing and extruding processes to produce a virucidal PP masterbatch through industrial-scale plastic compounding. PP, a durable thermoplastic polymer, holds a significant share of the global plastic market due to its widespread use in packaging and automotive applications [72]. Similar to the results observed with silicone composite, the PP masterbatch also exhibited excellent virucidal performance, maintaining its mechanical and thermal properties without significant deterioration. This was achieved by strategically positioning Cu_xO–TiO_2 near the PP surface rather than within the bulk material (Figs. S20–S23 and Tables S5 and S6).

3.4 Further application to virucidal NF filters

To demonstrate the broad applications of our virucidal materials, we developed an air filter by integrating Cu_xO–TiO_2 into a polymer solution and electrospinning it. Face masks, an essential personal protective equipment, play a key role in preventing the airborne transmission of infectious viruses. Conventional face mask filters rely on electrostatic absorption and repulsion to capture particulate matter [73]. Typically made of melt-blown fibers with diameters in the tens of micrometers, these filters capture charged particles, including aerosolized viruses. However, their efficacy can decrease in high-humidity conditions due to rapid neutralization of charged surfaces [74], reducing their ability to capture viruses. In contrast, electrospun NF air filters do not have this limitation. With a large surface area and fine pores, NF filters primarily use physical sieving to capture fine particles

[18, 75]. The robust fiber network within the NF structure also helps maintain filter integrity under mechanical strain.

Figure 5a shows SEM images of the electrospun NF filter and corresponding EDS elemental mappings of Ti and Cu, confirming the successful production of NFs with highly dispersed Cu_xO–TiO_2. As shown in Fig. 5b and c, the Cu_xO–TiO_2-infused NF filter exhibits Phi X 174 inactivation rate constants of 0.599 h^{-1} under dark conditions and 4.18 h^{-1} under visible light conditions. The sevenfold increase in virucidal performance under visible light indicates that the Cu_xO–TiO_2-infused NF filter is significantly enhanced by light, consistent with findings for silicone and PP products. Given the existing mass production capabilities for electrospun NF face masks, which use hundreds of nozzles and a roll-to-roll process, the virucidal Cu_xO–TiO_2 formulation can be easily implemented in large-scale manufacturing. This integration can also extend to various air filtration technologies, from face masks to air purifiers, improving indoor air quality.

4 Conclusion

The integration of Cu_xO–TiO_2 nanoparticles into polymer matrices presents a promising strategy for achieving sustained virucidal activity on commonly encountered surfaces, such as silicone, plastics, and air filters. Our study emphasizes the critical role of both the oxidation state and the local atomic structure of Cu species in enhancing virucidal performance. Under visible light irradiation, IFCT continuously generates active Cu_xO ($x > 1$) species, which significantly improves virucidal efficacy. When incorporated into polymer matrices like silicone, polypropylene (PP), and nanofiber (NF) filters, Cu_xO–TiO_2 exhibits exceptional virucidal activity while maintaining structural integrity and mechanical properties. This stability is attributed to surface segregation and controlled particle aggregation, ensuring the long-term effectiveness of the material. This study highlights the potential for large-scale production and application of Cu_xO–TiO_2 composites in polymer-based products and air filtration systems. Such materials can offer a durable and highly effective solution for mitigating the transmission of infectious viruses.

However, despite the promising results, certain challenges remain. One significant limitation is the charge separation in TiO_2, which may hinder efficient IFCT and reduce the overall photocatalytic antiviral efficiency. To address this limitation, we propose two key strategies for future investigation:

1. Incorporating plasmonic nanoparticles into the Cu_xO–TiO_2 composite to enhance visible–light responsiveness and improve charge transfer via plasmonic effects.
2. Doping TiO_2 with heteroatoms (e.g., nitrogen or carbon) to narrow its bandgap and increase sensitivity to longer wavelengths, thus improving its overall photocatalytic performance.

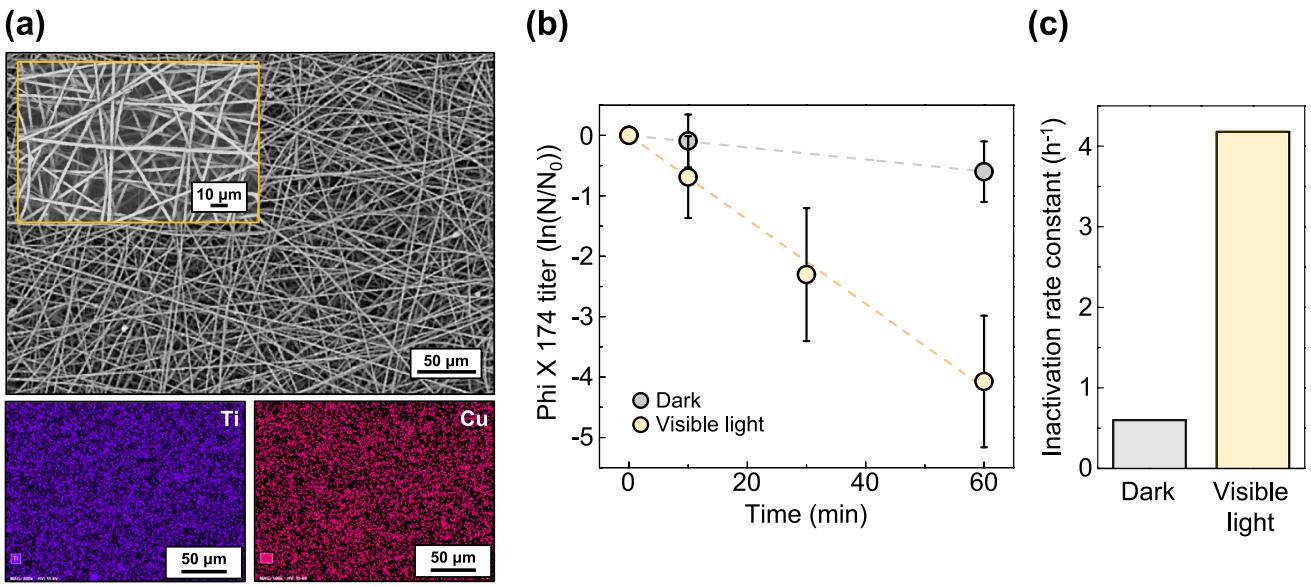

Fig. 5 Cu_xO–TiO_2-embedded PAN NF filter. **a** SEM image and the corresponding EDS elemental mapping results for Ti and Cu of Cu_xO–TiO_2-embedded NF filter. The inset figure shows an SEM image with high magnification. **b** Inactivation kinetics of Phi X 174 on the NF by Cu_xO–TiO_2 under dark and visible light conditions. **c** Inactivation rate constants calculated using the pseudo-first-order equation

These strategies aim to mitigate charge separation issues and optimize the photocatalytic activity of Cu_xO–TiO_2 composites, broadening their applicability for real-world scenarios. By implementing these approaches, we can further enhance the efficiency of Cu_xO–TiO_2 photocatalysts, facilitating their practical deployment in consumer products and contributing to the reduction of virus transmission.

Supplementary Information The online version contains supplementary material available at https://doi.org/10.1007/s42114-025-01383-1.

Acknowledgements The authors thank the Cooperative Equipment Center at KOREATECH, and Dr. Joohyun Kim, Dr. Juri Lee, and Professor Changha Lee for their advice and technical assistance with Phi X 174 culturing.

Author contribution Y. L., K. L., and J. S. contributed equally to this work. Y. L., K. L., and J. S. designed the experiments, performed the MD simulations, and wrote the original manuscript under the supervision of T. Y. K., I. N., and S. P., S. C., S. K., G. W. K., A. S., and J. W. H. conducted the data analyses and reviewed the original manuscript. T. Y. K., I. N., and S. P. conceived the concept and supervised the entire research. All authors discussed the results and participated in the preparation of the manuscript.

Funding This work was supported by the National Research Foundation of Korea (NRF) grant funded by the Korea government (MSIT) (No. RS-2022-NR073515, RS-2023–00212255, and RS-2023–00280278), the MSIT, Korea, under the ITRC support program (IITP-RS-2024–00436248) supervised by the IITP, and the National Institute of Supercomputing and Network/KISTI with supercomputing resources including technical support (KSC-2023-CRE-0364).

Data availability No datasets were generated or analysed during the current study.

Declarations

Conflict of interest The authors declare no competing interests.

References

1. Bogler A, Packman A, Furman A, Gross A, Kushmaro A et al (2020) Rethinking wastewater risks and monitoring in light of the COVID-19 pandemic. Nat Sustain 3:981–990. https://doi.org/10.1038/s41893-020-00605-2
2. Bandala ER, Kruger BR, Cesarino I, Leao AL, Wijesiri B, Goonetilleke A (2021) Impacts of COVID-19 pandemic on the wastewater pathway into surface water: a review. Sci Total Environ 774:145586. https://doi.org/10.1016/j.scitotenv.2021.145586
3. Meng QF, Tian R, Long H, Wu X, Lai J, Zharkova O, Wang JW, Chen X, Rao L (2021) Capturing cytokines with advanced materials: a potential strategy to tackle COVID-19 cytokine storm. Adv Mater 33:2100012. https://doi.org/10.1002/adma.202100012
4. Bashier H, Ikram A, Khan MA, Baig M, Al Gunaid M, Al Nsour M, Khader Y (2021) The anticipated future of public health services post COVID-19. JMIR Public Health Surveill 7:e26267. https://doi.org/10.2196/26267
5. World Health Organization (2022) WHO to identify pathogens that could cause future outbreaks and pandemics. https://www.who.int/news/item/21-11-2022-who-to-identify-pathogens-that-could-cause-future-outbreaks-and-pandemics. Accessed Sept 2024
6. Mishra B, Rath S, Mohanty M, Mohapatra PR (2023) The threat of impending pandemics: a proactive approach. Cureus 15:e33572. https://doi.org/10.7759/cureus.36723
7. The White House (2022) American pandemic preparedness plan: annual report. https://www.whitehouse.gov/ostp/news-updates/2022/09/01/fact-sheet-american-pandemic-preparedness-plan-annual-report/. Accessed Sept 2024
8. Marzoli F, Bortolami A, Pezzuto A, Mazzetto E, Piro R, Terregino C, Bonfante F, Belluco S (2021) A systematic review of human coronaviruses survival on environmental surfaces. Sci Total Environ 778:146191. https://doi.org/10.1016/j.scitotenv.2021.146191
9. Bak A, Mugglestone MA, Ratnaraja NV, Wilson JA, Rivett L, Stoneham SM, Bostock J, Moses SE, Price JR, Weinbren M, Loveday HP, Islam J, Wilson APR (2021) SARS-CoV-2 routes of transmission and recommendations for preventing acquisition: joint British infection association (BIA), healthcare infection society (HIS), infection prevention society (IPS) and royal college of pathologists (RCPath) guidance. J Hosp Infect 114:79–103. https://doi.org/10.1016/j.jhin.2021.04.027
10. Chia PY, Coleman KK, Tan YK, Ong SWX, Gum M, Lau SK, Lim XF, Lim AS, Sutjipto S, Lee PH, Son TT, Young BE, Milton DK, Gray GC, Schuster S, Barkham T, De PP, Vasoo S, Chan M, Ang BSP et al (2020) Detection of air and surface contamination by SARS–CoV–2 in hospital rooms of infected patients. Nat Commun 11:2800. https://doi.org/10.1038/s41467-020-16670-2
11. Ren G, Hu D, Cheng EW, Vargas-Reus MA, Reip P, Allaker RP (2009) Characterisation of copper oxide nanoparticles for antimicrobial applications. Int J Antimicrob Agents 33:587–590. https://doi.org/10.1016/j.ijantimicag.2008.12.004
12. Yoon KY, Byeon JH, Park JH, Hwang J (2007) Susceptibility constants of *Escherichia coli* and *Bacillus subtilis* to silver and copper nanoparticles. Sci Total Environ 373:572–575. https://doi.org/10.1016/j.scitotenv.2006.11.007
13. van Doremalen N, Bushmaker T, Morris DH, Holbrook MG, Gamble A, Williamson BN, Tamin A, Harcourt JL, Thornburg NJ, Gerber SI, Lloyd-Smith JO, de Wit E, Munster VJ (2020) Aerosol and surface stability of SARS–CoV–2 as compared with SARS–CoV–1. N Engl J Med 382:1564–1567. https://doi.org/10.1056/NEJMc2004973
14. Kim SJ (2021) A case study on performance analysis of antimicrobial copper film attaching to window for responding to COVID-19 and others. J Korean Soc Disaster Secur 14:23−40. https://doi.org/10.21729/ksds.2021.14.1.23
15. Imlay JA (2003) Pathways of oxidative damage. Annu Rev Microbiol 57:395–418. https://doi.org/10.1146/annurev.micro.57.030
16. Miyauchi M, Sunada K, Hashimoto K (2020) Antiviral effect of visible light-sensitive Cu–O/TiO_2 photocatalyst. Catalysts 10:1093. https://doi.org/10.3390/catal10091093

17. Thurman RB, Gerba CP, Bitton G (1989) The molecular mechanisms of copper and silver ion disinfection of bacteria and viruses. Crit Rev Environ Sci Technol 18:295–315. https://doi.org/10.1080/10643388909388351
18. Yoon J, Kim J, Lee J, Hong SP, Park S, Jeong YW, Lee C, Oh SG (2022) Fabrication of antiviral nanofibers containing various Cu salts and ZnO nanorods by electrospinning. J Ind Eng Chem 116:572–580. https://doi.org/10.1016/j.jiec.2022.09.045
19. Sunada K, Minoshima M, Hashimoto K (2012) Highly efficient antiviral and antibacterial activities of solid-state cuprous compounds. J Hazard Mater 235:265–270. https://doi.org/10.1016/j.jhazmat.2012.07.052
20. Minoshima M, Lu Y, Kimura T, Nakano R, Ishiguro H, Kubota Y, Hashimoto K, Sunada K (2016) Comparison of the antiviral effect of solid-state copper and silver compounds. J Hazard Mater 312:1–7. https://doi.org/10.1016/j.jhazmat.2016.03.023
21. Qiu X, Miyauchi M, Sunada K, Minoshima M, Liu M, Lu Y, Li D, Shimodaira Y, Hosogi Y, Kuroda Y, Hashimoto K (2012) Hybrid Cu_xO/TiO_2 nanocomposites as risk–reduction materials in indoor environments. ACS Nano 6:1609–1618. https://doi.org/10.1021/nn2045888
22. Jampa S, Ratanatawanate C, Pimtong W, Aueviriyavit S, Chantho V, Sillapaprayoon S, Kunyanee C, Warin C, Gamonchuang J, Kumnorkaew P (2022) Transparent anti-SARS-CoV-2 film from copper(I) oxide incorporated in zeolite nanoparticles. ACS Appl Mater Interfaces 14:52334–52346. https://doi.org/10.1021/acsami.2c12274
23. Merkl P, Long S, McInerney GM, Sotiriou GA (2021) Antiviral activity of silver, copper oxide and zinc oxide nanoparticle coatings against SARS-CoV-2. Nanomaterials 11:1312. https://doi.org/10.3390/nano11051312
24. Irie H, Miura S, Kamiya K, Hashimoto K (2008) Efficient visible light-sensitive photocatalysts: grafting Cu(II) ions onto TiO_2 and WO_3 photocatalysts. Chem Phys Lett 457:202–205. https://doi.org/10.1016/j.cplett.2008.04.006
25. Liu M, Sunada K, Hashimoto K, Miyauchi M (2015) Visible-light sensitive Cu(II)–TiO_2 with sustained anti-viral activity for efficient indoor environmental remediation. J Mater Chem A 3(33):17312–17319. https://doi.org/10.1039/c5ta03756e
26. Sunada K, Watanabe T, Hashimoto K (2003) Bactericidal activity of copper-deposited TiO_2 thin film under weak UV light illumination. Environ Sci Technol 37:4785–4789. https://doi.org/10.1021/es034106g
27. Liu M, Inde R, Nishikawa M, Qiu X, Atarashi D, Sakai E, Nosaka Y, Hashimoto K, Miyauchi M (2014) Enhanced photoactivity with nanocluster-grafted titanium dioxide photocatalysts. ACS Nano 8:7229–7238. https://doi.org/10.1021/nn502247x
28. Kim J, Lee J, Kim S, Kim T, Lee KM, Lee D, Cho J, Kim JY, Jeong YW, Park HJ, Lee JC, Lee C (2024) Virucidal activity of Cu-doped TiO_2 nanoparticles under visible light illumination: effect of Cu oxidation state. J Hazard Mater 465:133525. https://doi.org/10.1016/j.jhazmat.2024.133525
29. Nakano R, Yamaguchi A, Sunada K, Nagai T, Nakano A, Suzuki Y, Yano H, Ishiguro H, Miyauchi M (2022) Inactivation of various variant types of SARS-CoV-2 by indoor-light-sensitive TiO_2-based photocatalyst. Sci Rep 12:5804. https://doi.org/10.1038/s41598-022-09402-7
30. Cartwright A, Jackson K, Morgan C, Anderson A, Britt DW (2020) A review of metal and metal-oxide nanoparticle coating technologies to inhibit agglomeration and increase bioactivity for agricultural applications. Agronomy 10(7):1018. https://doi.org/10.3390/agronomy10071018
31. Cinteză LO, Tănase MA (2020) Multifunctional ZnO nanoparticle-based coatings for cultural heritage preventive conservation. In: Ares AE (ed) Thin Films. IntechOpen, pp 1–20. https://doi.org/10.5772/intechopen.94070
32. Rapp MV, Donaldson SH Jr, Gebbie MA, Das S, Kaufman Y, Gizaw Y, Koenig P, Roiter Y, Israelachvili JN (2015) Hydrophobic, electrostatic, and dynamic polymer forces at silicone surfaces modified with long–chain bolaform surfactants. Small 11:2058–2068. https://doi.org/10.1002/smll.201402229
33. Irie H, Kamiya K, Shibanuma T, Miura S, Tryk DA, Yokoyama T, Hashimoto K (2009) Visible light-sensitive Cu(II)–grafted TiO_2 photocatalysts: activities and X-ray absorption fine structure analyses. J Phys Chem C Nanomater Interfaces 113:10761–10766. https://doi.org/10.1021/jp903063z
34. Wach A, Zou X, Wojtaszek K, Kayser Y, Garlisi C, Palmisano G, Sá J, Szlachetko J (2023) Towards understanding the TiO_2 doping at the surface and bulk. X-Ray Spectrom 52:261–268. https://doi.org/10.1002/xrs.3363
35. Nguyen TH, Nguyen TL, Ung TDT, Nguyen QL (2013) Synthesis and characterization of nano–CuO and CuO/TiO_2 photocatalysts. Adv Nat Sci Nanosci Nanotechnol 4:025002. https://doi.org/10.1088/2043-6262/4/2/025002
36. Baek J, Park S, Song CK, Kim TY, Nam I, Lee JM, Han JW, Yi J (2015) Radial alignment of c-channel nanorods in 3D porous TiO_2 for eliciting enhanced Li storage performance. Chem Commun 51:15019–15022. https://doi.org/10.1039/C5CC04864H
37. Miyauchi M, Liu Z, Zhao ZG, Anandan S, Tokudome H (2010) Visible light-driven superhydrophilicity by interfacial charge transfer between metal ions and metal oxide nanostructures. Langmuir 26:796–801. https://doi.org/10.1021/la902177x
38. Choudhury B, Dey M, Choudhury A (2013) Defect generation, d–d transition, and band gap reduction in Cu-doped TiO_2 nanoparticles. Int Nano Lett 3:1–8. https://doi.org/10.1186/2228-5326-3-25
39. Ozdemir KG, Yılmaz H, Yılmaz S (2009) In vitro evaluation of cytotoxicity of soft lining materials on L929 cells by MTT assay. J Biomed Mater Res B Appl Biomater 90:82−86. https://doi.org/10.1002/jbm.b.31256
40. U.S. Food & Drug Administration (2024) Impact of nanoscale TiO_2 and ZnO used in sunscreens on skin bacteria. https://www.fda.gov/science-research/fda-science-forum/impact-nanoscale-TiO2-and-zno-used-sunscreens-skin-bacteria. Accessed Sept 2024
41. U.S. Food & Drug Administration (2024) Titanium dioxide as a color additive in foods. https://www.fda.gov/industry/color-additives/titanium-dioxide-color-additive-foods. Accessed Sept 2024
42. Miyauchi M, Irie H, Liu M, Qiu X, Yu H, Sunada K, Hashimoto K (2016) Visible–light–sensitive photocatalysts: nanocluster-grafted titanium dioxide for indoor environmental remediation. J Phys Chem Lett 7:75–84. https://doi.org/10.1021/acs.jpclett.5b02041
43. Okamoto Y, Kubota T, Gotoh H, Ohto Y, Aritani H, Tanaka T, Yoshida S (1998) XAFS study of zirconia–supported copper catalysts for the NO–CO reaction: deactivation, rejuvenation and stabilization of Cu species. J Chem Soc Faraday Trans 94:3743–3752. https://doi.org/10.1039/A807152G
44. Rezende LF, Willcox S, Griffith JD, Richardson CC (2003) A single-stranded DNA-binding protein of bacteriophage T7 defective in DNA annealing. J Biol Chem 278(31):29098–29105. https://doi.org/10.1074/jbc.M303374200
45. Son T, Cho YJ, Lee H, Cho MY, Goh B, Kim HM, Hoa PTN, Cho SH, Park YJ, Park HS, Hong KS (2022) Monitoring in vivo behavior of size-dependent fluorescent particles as a model fine dust. J Nanobiotechnol 20:227. https://doi.org/10.1186/s12951-022-01419-4
46. Isaacs MA, Davies-Jones J, Davies PR, Guan S, Lee R, Morgan DJ, Palgrave R (2021) Advanced XPS characterization: XPS-based multi-technique analyses for comprehensive understanding of functional materials. Mater Chem Front 5:7931–7963. https://doi.org/10.1039/D1QM00969A
47. Hofstetter YJ, Vaynzof Y (2019) Quantifying the damage induced by X-ray photoelectron spectroscopy depth profiling of organic

conjugated polymers. ACS Appl Polym Mater 1:1372–1381. https://doi.org/10.1021/acsapm.9b00148
48. Mack P (n.d.) Monatomic and cluster argon ion XPS depth profiling of $SrTiO_3$ and HfO_2. https://assets.thermofisher.com/TFS-Assets/MSD/Scientific-Resources/Monatomic-Cluster-Argon-Ion-XPS-Presentation.pdf. Accessed 14 Mar 2025
49. Miyauchi M, Nakajima A, Watanabe T, Hashimoto K (2002) Photocatalysis and photoinduced hydrophilicity of various metal oxide thin films. Chem Mater 14:2812–2816. https://doi.org/10.1021/cm020076p
50. Simovic S, Prestidge CA (2003) Hydrophilic silica nanoparticles at the PDMS droplet−water interface. Langmuir 19:3785–3792. https://doi.org/10.1021/la026803c
51. Kanduč M, Schlaich A, Schneck E, Netz RR (2016) Water-mediated interactions between hydrophilic and hydrophobic surfaces. Langmuir 32:8767–8782. https://doi.org/10.1021/acs.langmuir.6b01727
52. Bell NS, Frischknecht AL, Piech M (2010) Grafted low molecular weight polymers as steric stabilizers of commercial titania nanoparticles in polydimethylsiloxane fluids. J Dispersion Sci Technol 32:128–140. https://doi.org/10.1080/01932691003656789
53. Croll S (2002) DLVO theory applied to TiO_2 pigments and other materials in latex paints. Prog Org Coat 44:131–146. https://doi.org/10.1016/S0300-9440(01)00261-2
54. Hua Z, Zhang J, Bai X, Ye Z, Tang Z, Liang L, Liu Y (2016) Aggregation of TiO_2–graphene nanocomposites in aqueous environment: influence of environmental factors and UV irradiation. Sci Total Environ 539:196–205. https://doi.org/10.1016/j.scitotenv.2015.08.143
55. Sharma PK, Gupta N, Dankov PI (2020) Characterization of polydimethylsiloxane (PDMS) as a wearable antenna substrate using resonance and planar structure methods. AEU 127:153455. https://doi.org/10.1016/j.aeue.2020.153455
56. Lu Y, Hu GH (2021) A potential barrier in the diffusion of nanoparticles in ordered polymer networks. Soft Matter 17:6374–6382. https://doi.org/10.1039/D1SM00018G
57. International Organization for Standardization (2011) Measurement of antibacterial activity on plastics and other nonporous surfaces; ISO 22196:2011. https://www.iso.org/standard/54431.html. Accessed Sept 2024
58. Chiappara C, Arrabito G, Ferrara V, Scopelliti M, Sancataldo G, Vetri V, Chillura Martino DF, Pignataro B (2021) Improved photocatalytic activity of polysiloxane TiO_2 composites by thermally induced nanoparticle bulk clustering and dye adsorption. Langmuir 37:10354–10365. https://doi.org/10.1021/acs.langmuir.1c01475
59. Ma K, Yehezkeli O, He L, Cha JN (2018) DNA for assembly and charge transport photocatalytic reduction of CO_2. Adv Sustain Syst 2:1700156. https://doi.org/10.1002/adsu.201700156
60. Qin Y, Chen X, Zhao Z, Pu C (2024) Assembled quantum dot porous clusters for enhanced photocatalytic reduction of quinone to hydroquinone. ACS Catal 14:1243–1251. https://doi.org/10.1021/acscatal.3c04492
61. Ni J, Wang Y, Zhang H, Sun JZ, Tang BZ (2021) Aggregation-induced generation of reactive oxygen species: mechanism and photosensitizer construction. Molecules 26:268. https://doi.org/10.3390/molecules26020268
62. Pellegrino F, Pellutiè L, Sordello F, Minero C, Ortel E, Hodoroaba V-D, Maurino V (2017) Influence of agglomeration and aggregation on the photocatalytic activity of TiO_2 nanoparticles. Appl Catal B Environ 216:80–87. https://doi.org/10.1016/j.apcatb.2017.05.046
63. Tolosana-Moranchel A, Pecharromán C, Faraldos M, Bahamonde A (2021) Strong effect of light scattering by distribution of TiO_2 particle aggregates on photocatalytic efficiency in aqueous suspensions. Chem Eng J 403:126186. https://doi.org/10.1016/j.cej.2020.126186
64. Jassby D, Farner Budarz J, Wiesner M (2012) Impact of aggregate size and structure on the photocatalytic properties of TiO_2 and ZnO nanoparticles. Environ Sci Technol 46:6934–6941. https://doi.org/10.1021/es202009h
65. Lee J, Kim J, Kim S, Kim T, Lee KM, Cho J, Choi JW, Kim JY, Jeong YW, Park HJ, Lee C (2025) Enhanced virucidal activity of facet-engineered Cu-doped TiO_2 nanorods under visible light illumination. Water Res 268:122579. https://doi.org/10.1016/j.watres.2024.122579
66. Endo-Kimura M, Karabiyik B, Wang K, Wei Z, Ohtani B, Markowska-Szczupak A, Kowalska E (2020) Vis-responsive copper-modified titania for decomposition of organic compounds and microorganisms. Catalysts 10:1194. https://doi.org/10.3390/catal10101194
67. De Lima MS, Schio AL, Aguzzoli C, De Souza WV, Roesch-Ely M, Leidens LM, Michels AF (2024) Visible light-driven photocatalysis and antibacterial performance of a Cu–TiO_2 nanocomposite. ACS Omega 9:47122–47134. https://doi.org/10.1021/acsomega.4c07515
68. Naumenko K, Zahorodnia S, Pop CV, Rizun N (2023) Antiviral activity of silver nanoparticles against the influenza A virus. J Virus Erad 9(2):100330. https://doi.org/10.1016/j.jve.2023.100330
69. Kumar SR, Paulpandi M, ManivelRaja M, Mangalaraj D, Viswanathan C, Kannan S, Ponpandian N (2014) An in vitro analysis of H1N1 viral inhibition using polymer coated superparamagnetic Fe_3O_4 nanoparticles. RSC Adv 4(26):13409–13418. https://doi.org/10.1039/C3RA47542E
70. KA S, N J, K VR (2024) Zinc oxide-based antibacterial and anti-viral functional materials. In: Antibacterial and Antiviral Functional Materials, Volume 2. American Chemical Society, pp 281–307. https://doi.org/10.1021/bk-2024-1472.ch009
71. Ghezzi S, Pagani I, Poli G, Pal S, Licciulli A, Perboni S, Vicenzi E (2020) Rapid inactivation of SARS-CoV-2 by coupling tungsten trioxide (WO_3) photocatalyst with copper nanoclusters. J Nanotechnol Nanomater 1(3):109–115. https://doi.org/10.33696/Nanotechnol.1.014
72. Hossain MT, Shahid MA, Mahmud N, Habib A, Rana MM, Khan SA, Hossain MD (2024) Research and application of polypropylene: a review. Discover Nano 19:1–21. https://doi.org/10.1186/s11671-023-03952-z
73. Wang Y, Deng Z, Shi D (2021) How effective is a mask in preventing COVID-19 infection? Med Devices Sensors 4:e10163
74. Liu C, Dai Z, He B, Ke QF (2020) The effect of temperature and humidity on the filtration performance of electret melt–blown nonwovens. Mater 13:4774. https://doi.org/10.3390/ma13214774
75. Ji X, Huang J, Teng L, Li S, Li X, Cai W, Chen Z, Lai Y (2023) Advances in particulate matter filtration: materials, performance, and application. Green Energy Environ 8:673–697. https://doi.org/10.1016/j.gee.2022.03.012